frontiers | Frontiers in Materials

TYPE Original Research
PUBLISHED 21 September 2022
DOI 10.3389/fmats.2022.1015839

OPEN ACCESS

EDITED BY
Fuyin Ma,
Xi'an Jiaotong University, China

REVIEWED BY
Fengxian Xin,
Xi'an Jiaotong University, China
Zhibao Cheng,
Beijing Jiaotong University, China

*CORRESPONDENCE
Honggang Zhao,
zhhg9603@sina.com
Jihong Wen,
wenjihong@vip.sina.com

SPECIALTY SECTION
This article was submitted to Metamaterials, a section of the journal Frontiers in Materials

RECEIVED 10 August 2022
ACCEPTED 22 August 2022
PUBLISHED 21 September 2022

CITATION
Wang C, Zhao H, Wang Y, Zhong J, Yang H, Yu D and Wen J (2022), Low-frequency waterborne sound insulation by an acoustic metascreen with a metal chiral structure.
Front. Mater. 9:1015839.
doi: 10.3389/fmats.2022.1015839

Low-frequency waterborne sound insulation by an acoustic metascreen with a metal chiral structure

Chao Wang[1,2], Honggang Zhao[1,2]*, Yang Wang[1,2], Jie Zhong[1,2], Haibin Yang[1,2], Dianlong Yu[1,2] and Jihong Wen[1,2]*

[1]College of Intelligence Science and Technology, National University of Defense Technology, Changsha, China, [2]Laboratory of Science and Technology on Integrated Logistics Support, National University of Defense Technology, Changsha, China

Low sound speed or low-density materials can be used as soft acoustic boundaries in water, potentially as low-frequency underwater sound insulation. This study uses a chiral structure to construct an acoustic metascreen with deep subwavelength thickness. The results show that the transmission coefficient of the metascreen decreases noticeably in the low-frequency range when adjusting the chiral structure. The displacement pattern and the effective acoustic impedance are used to investigate the sound insulation mechanism. Low sound speed and effective acoustic impedance are found in the anisotropic chiral structure, and an extensive range of quasi-longitudinal wave phase velocities from 116.70 m/s to 3935.48 m/s can be obtained by adjusting the structural parameters without changing the filling rate. Finally, the effect of the oblique incidence angle on the sound insulation of the metascreen is investigated.

KEYWORDS

acoustic metascreen, chiral structure, underwater sound insulation, homogenization, effective parameter

Introduction

The use of acoustic metascreens (Leroy et al., 2009; Leroy et al., 2015) has great significance in shielding unwanted noise radiation from underwater equipment to reduce the interference of underwater acoustic communication and prevent sonar detection (Hladky-Hennion and Decarpigny, 1991; Zhang et al., 2013; Lanoy et al., 2018; Chen Y. et al., 2020; Wu et al., 2020; Dong et al., 2021).

Conventionally, the design paradigm of the acoustic metascreen is using a soft material (e.g., silicon rubber) embedded periodically with cavities (Leroy et al., 2015). Calvo et al. (2015) designed a metascreen by embedding monolayer and multilayer arrays of disk-shaped cavities into rubber. Results showed that sound attenuation is evident near the monopole resonance frequency of the cavity, and disk-shaped cavities have more sound insulation advantages than near-spherical cavities. Yang et al. (2019) proposed a metascreen made of periodically perforated rubber layers with metal plates and revealed

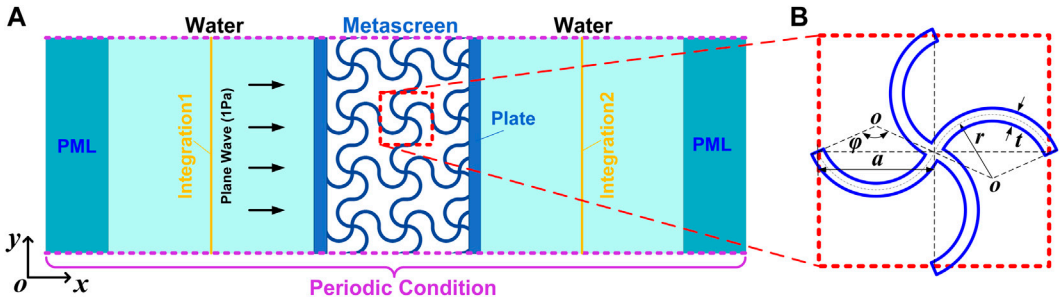

FIGURE 1
(A) Finite element model of sound transmission through a two-dimensional acoustic metascreen. **(B)** Schematic diagram of a unit cell from the metascreen.

the sound insulation mechanism using the complex band mechanism. Cai et al. (2019) developed a general method to construct three-dimensional (3D)-soft metascreen using bubbles as local resonance units in a 3D-printed frame. The experimental results showed that the obstruction of underwater sound in a wide frequency range from 2 to 26 kHz was achieved. However, insulation for underwater sound at frequencies below 2 kHz has been less explored because of the high penetrability of long wavelengths.

Compared with the above metascreens based on local resonance or Bragg scattering, recent reports show that the metascreens based on a functional lattice can provide new design paradigms for low-frequency broadband waterborne sound insulation (Chen Z. et al., 2020; Wang et al., 2022; Zhao et al., 2022). It was found that bi-mode materials with optimal azimuth are favorable for achieving extremely low acoustic impedance, displaying efficient sound insulation in low-frequency domains. Strong anisotropy is required when bi-mode materials possess a positive Poisson's ratio. By contrast, weak anisotropy benefits for low acoustic impedance when bi-mode materials have a negative Poisson's ratio. However, whether materials without bi-mode characteristics can achieve low-acoustic impedances remains an open question.

Recently, chiral structures have attracted growing interest in designing mechanical and thermal metamaterials with intriguing phenomena like negative Poisson's ratios (Lakes et al., 2015; Wu et al., 2019; Liu et al., 2021; Yin et al., 2021). Chiral structures have recently also been introduced to underwater sound absorption (An et al., 2021). However, to our knowledge, the characteristics of low acoustic impedance and low sound speed of chiral structure have not been investigated.

This study introduces an anisotropic chiral structure made of aluminum with high density and elastic modulus as underwater sound insulation. A lower sound speed effect, resulting in lower effective acoustic impedance, is found in this anisotropic chiral structure with a metal matrix. The sound insulation mechanism of the acoustic metascreen is revealed using effective parameters and displacement patterns. Finally, the effect of incidence angle on the sound insulation of the acoustic metascreen is discussed.

Model and simulation method

This work considers two-dimensional acoustic wave propagation between water and a metascreen in a Cartesian coordinate system. As illustrated in Figure 1A, a harmonic plane wave is incident on the metascreen along the x direction from the left semi-infinite water domain. The metascreen is comprises two cover plate panels embedded with periodically anisotropic chiral structures.

The unit cell of the chiral structure is shown in Figure 1B. The unit cell consists of four identical arc beams connected at the head and distributed with rotational symmetry around the center junction. The chiral structure is characterized by four main parameters: the central angle φ, beam thickness t, arc radius r, and lattice constant $2a$. For $0° < \varphi \leq 360°$, $a = 2rsin(\varphi/2)$. The structure's degree of chirality is increased with increasing central angle φ. It should be noted that when φ approaches 0°, the corresponding arc beam approximates a straight line, and a square honeycomb lattice unit cell is utilized to deal with this extreme situation for the chiral structure. The filling rate of this chiral structure is defined as the ratio of the volume of solid material (V_s) to the unit cell volume (V_{cell}), and is given by

$$\Phi = \frac{V_s}{V_{cell}} = \begin{cases} \dfrac{4at - t^2}{4a^2}, & \varphi = 0° \\ \dfrac{\pi \cdot 2r \cdot t}{a^2} \cdot \dfrac{\varphi}{360°}, & 0° < \varphi \leq 360° \end{cases} \tag{1}$$

Full-wave simulations are performed using the Acoustic Solid interaction, Frequency Domain Interface of the COMSOL Multiphysics to evaluate the metascreens' sound insulation capabilities. In the numerical model, the acoustic metascreen, which is infinite in the y direction, is modeled using the Solid Mechanics module, and the water domain is modeled using the Acoustic module.

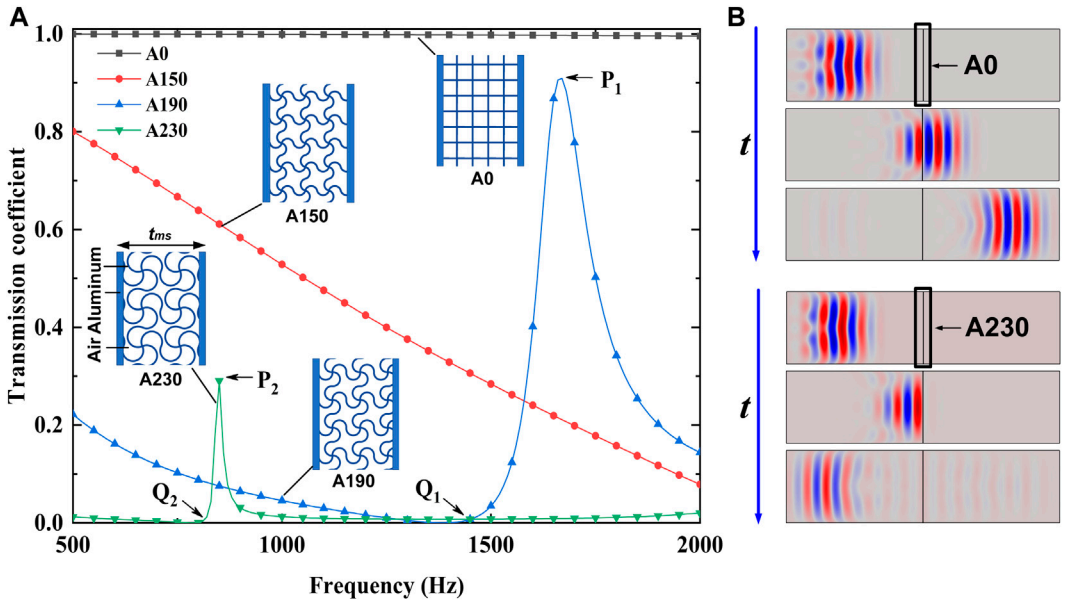

FIGURE 2
(A) The variation of the metascreen transmission coefficient frequency for different central angles φ. The inset diagrams show the A0, A150, A190, and A230 metascreens. **(B)** The time-domain sound transmission of A0 and A230 for an incident transient Gaussian pulse.

TABLE 1 Structural parameters of four metascreens.

Metascreen	φ/(°)	a/(mm)	r/(mm)	t/(mm)
A0	0	3.03	-	0.7
A150	150	4.36	2.26	0.7
A190	190	5.36	2.69	0.7
A230	230	7.13	3.93	0.7

Acoustic structural boundaries are applied to the two interfaces between the metascreen and water. Both horizontal purple dashed lines in Figure 1A represent periodic boundaries. A plane wave with 1 Pa amplitude is incident on the metascreen from the left side of the water domain. Both outer boundaries are set to perfectly matched layer (PML) conditions to simulate anechoic termination for the scattering wave. The transmission coefficient of sound energy is calculated using the ratio of the integral of the incident and transmitted sound fields at the solid yellow lines in Figure 1A.

Sound transmission of typical metascreens

Figure 2A compares the transmission coefficients of the metascreens embedded with different chiral structures. Here the metascreens are denoted as A0, A150, A190, and A230 for chiral structures with central angles ofφ = 0°, 150°, 190°, and 230°, respectively. Note that the A0 metascreen, which consists of a square honeycomb lattice, is not strictly chiral and is included for comparison. Table 1 lists the specific structural parameters of the metascreens. All metascreens have the same overall thicknesst_{ms} = 32.52 mm and filling rate Φ = 0.2174. The thickness of the cover plate is t_{plate} = 2 mm. The metascreen material is aluminum with mass densityρ_{Al} = 2700 kg/m^3, Young's modulus E_{Al} = 69 GPa and Poisson's ratio ν_{Al} = 0.33. The mass density and longitudinal wave speed of water are ρ_w = 1000 kg/m^3 and c_w = 1500 m/s, respectively. The frequency ranges from 500 to 2000 Hz (equivalent to $23t_{ms} \le \lambda = c_w/f \le 92t_{ms}$) is considered in the simulations.

From Figure 2A, one can see that the metascreen transmission coefficient in the low-frequency band decreases noticeably with increasing central angle φ, meaning the sound insulation performance of the metascreen at low frequency improves significantly as the degree of chirality of the structure increases. The average transmission coefficient of A230 in the 500–2000 Hz frequency range is only 0.0145, which means almost 98.55% of the incident sound energy is isolated. However, A0 is almost transparent to underwater sound. Metascreens A190 and A230 both show narrow band transmission peaks that are denoted P_1 (1,666 Hz) and P_2 (853 Hz), respectively. In the considered frequency band, both metascreens also have transmission valleys, denoted Q_1 (1,385 Hz) and Q_2 (791 Hz), respectively.

Time-domain simulations are carried out to display the sound insulation performance of the acoustic metascreen more intuitively. The incidence of a Gaussian pulse with frequency around $f_0 = 700$ Hz with time duration $\Delta T = 2.9$ ms is used. The transient response ($t = 9.5$ ms, $t = 15.5$ ms, and $t = 22$ ms) of metascreens A0 and A230 in the time domain are compared in Figure 2B. The incident wave is almost unchanged as it passes through metascreen A0, demonstrating it is transparent to underwater sound. However, the incident wave is almost entirely reflected by metascreen A230, demonstrating that it can block almost all incident sound energy.

Theoretical method

The homogenization method (Bensoussan and Alain, 1978; Cheng et al., 2013) based on a unit cell is used to obtain the effective parameters of the chiral structures, which mainly determine the effective metascreen properties. According to the homogenization theory, the fourth effective elastic tensor of the chiral lattice material is

$$\boldsymbol{C}^H = \begin{bmatrix} C^H_{1111} & C^H_{1122} & C^H_{1112} \\ C^H_{1122} & C^H_{2222} & C^H_{2212} \\ C^H_{1112} & C^H_{2212} & C^H_{1212} \end{bmatrix}, \tag{2}$$

which can be calculated by

$$C^H_{ijkl} = \frac{1}{|Y|}\int_Y C^H_{pqrs}\left(\varepsilon^{0(ij)}_{pq} - \varepsilon^{(ij)}_{pq}\right)\left(\varepsilon^{0(kl)}_{rs} - \varepsilon^{(kl)}_{rs}\right)dY, \tag{3}$$

where $|Y|$ is the area of a two-dimensional unit cell or the volume of a three-dimensional unit cell, C^H_{pqrs} is the inherent elastic tensor of solid material (i, j, k, l and p, q, r, $s = 1$ or 2), and $\varepsilon^{0(ij)}_{pq}$ is the unit test strain field of loading. $\varepsilon^{(kl)}_{pq}$ represents the strain response and can be expressed as a function of the displacement field χ^{kl}:

$$\varepsilon^{(kl)}_{pq} = \frac{1}{2}\left(\chi^{kl}_{p,q} + \chi^{kl}_{q,p}\right). \tag{4}$$

In addition, the displacement field χ^{kl} can be solved from the following expression

$$\int_Y \varepsilon_{ij}(\boldsymbol{v}) C^H_{ijpq}\varepsilon_{pq}\left(\chi^{kl}\right)\, dY = \int_Y \varepsilon_{ij}(\boldsymbol{v}) C^H_{ijpq}\varepsilon^{0(kl)}_{pq}\, dY, \tag{5}$$

where $\boldsymbol{v}$ is the virtual displacement field. Using the finite element method and additional periodic boundaries of the unit, the discrete form of Eq. 5 can be expressed as

$$\boldsymbol{K}\boldsymbol{\chi}^n = \boldsymbol{F}^n, \tag{6}$$

where $\boldsymbol{K} = \sum_{e=1}^N \boldsymbol{k}_e = \sum_{e=1}^N \int_{V_e} \boldsymbol{B}_e^T \boldsymbol{D}_e \boldsymbol{B}_e dV_e$ is the stiffness matrix, $\boldsymbol{\chi}^n$ is the displacement field, $\boldsymbol{F}^n = \sum_{e=1}^N \int_{V_e} \boldsymbol{B}_e^T \boldsymbol{D}_e \boldsymbol{\varepsilon}^n dV_e$ is the load, N denotes the number of discrete elements, $\boldsymbol{k}_e$ is the stiffness matrix of the eth element, $\boldsymbol{B}_e$ represents the strain displacement matrix, and $\boldsymbol{\varepsilon}^n$ refers to the independent strain field. The loading strain fields are $\varepsilon^1 = [1\ 0\ 0]^T$, $\varepsilon^2 = [0\ 1\ 0]^T$ and $\varepsilon^3 = [0\ 0\ 1]^T$, respectively. $\boldsymbol{D}_e$ is the constitutive matrix of the element in the plane strain problem:

$$\boldsymbol{D}_e = \frac{E_e}{(1+\nu_e)(1-2\nu_e)}\begin{bmatrix} 1-\nu_e & \nu_e & 0 \\ \nu_e & 1-\nu_e & 0 \\ 0 & 0 & \dfrac{(1-2\nu_e)}{2} \end{bmatrix}, \tag{7}$$

where E_e and ν_e denote Young's modulus and Poisson's ratio, respectively, of each element. After obtaining $\boldsymbol{\chi}^n$ from Eq. 6, the effective fourth-order elastic tensor of the unit cell can be found from

$$\boldsymbol{C}^H = \frac{1}{|Y|}\sum_{e=1}^N \int_{V_e} \left(\boldsymbol{I} - \boldsymbol{B}_e\boldsymbol{\chi}_e\right)^T \boldsymbol{D}_e \left(\boldsymbol{I} - \boldsymbol{B}_e\boldsymbol{\chi}_e\right) dV_e, \tag{8}$$

where $\boldsymbol{B}_e\boldsymbol{\chi}_e$ denotes the strains caused by the distribution of non-uniform materials. In addition, the effective density ρ_s of a unit cell is identical to the average density of the solid.

The effective parameters of the metascreens at low frequency can then be calculated as follows (Chen Y. et al., 2020; Wang et al., 2022):

$$c_{qL} = \sqrt{\frac{C^H_{1111} + C^H_{1212} + \sqrt{\left(C^H_{1111} - C^H_{1212}\right)^2 + 4C^H_{1112}2}}{2\rho_s}}, \tag{9}$$

$$c_{qT} = \sqrt{\frac{C^H_{1111} + C^H_{1212} - \sqrt{\left(C^H_{1111} - C^H_{1212}\right)^2 + 4C^H_{1112}2}}{2\rho_s}}, \tag{10}$$

$$\theta_{qL} = tan^{-1}\frac{2C^H_{1112}}{C^H_{1111} - C^H_{1212} + \sqrt{\left(C^H_{1111} - C^H_{1212}\right)^2 + 4C^H_{1112}2}}, \tag{11}$$

$$\theta_{qT} = tan^{-1}\frac{2C^H_{1112}}{C^H_{1111} - C^H_{1212} - \sqrt{\left(C^H_{1111} - C^H_{1212}\right)^2 + 4C^H_{1112}2}}, \tag{12}$$

where, c_{qL} and c_{qT} represent the phase velocities of quasi-longitudinal (qL) and quasi-transverse (qT) waves in anisotropic solids, respectively. θ_{qL} and θ_{qT} are the polarization angles between the vibration direction of the particles and the wave vectors of both wave modes. For anisotropic solids, the qL and qT wave modes are excited at the same time under the condition of normal incidence. Then, the polarization factor η and effective acoustic impedance Z_{eff} can be further obtained from

$$\eta = \frac{c_{qT} + c_{qT}tan^2\theta_{qL}}{c_{qT} + c_{qL}tan^2\theta_{qL}}, \tag{13}$$

$$Z_{eff} = \rho_s c_{qL}\eta. \tag{14}$$

Results and discussion

To intuitively observe the variation of the unit cell with the degree of chirality, Figure 3 shows the unit cells for increasing

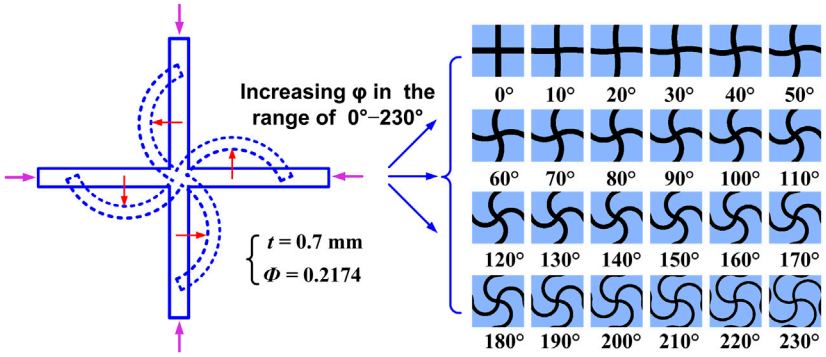

FIGURE 3
Unit cells obtained for central angles φ between 0° and 230°.

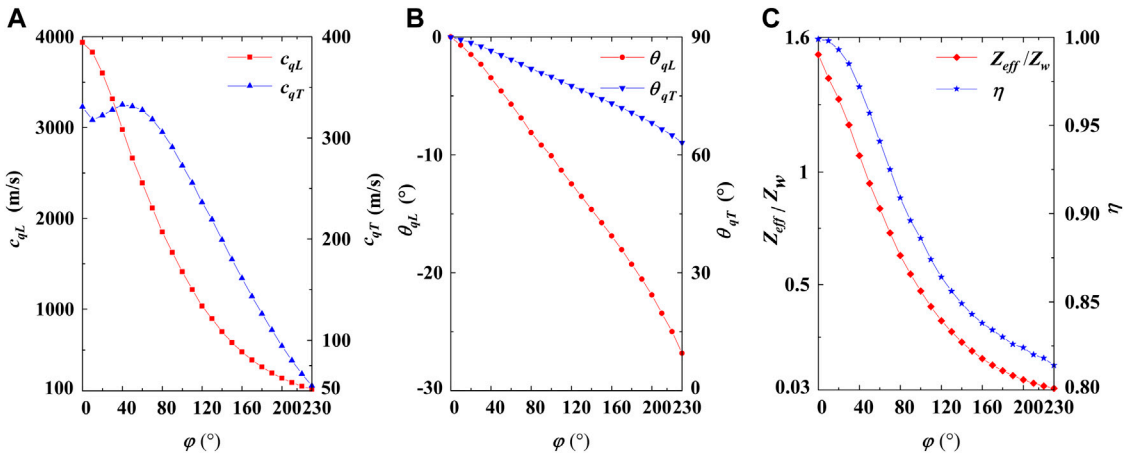

FIGURE 4
(A) The variation in phase velocities of the qL wave (c_{qL}) and the qT wave (c_{qT}) of the metascreens with central angle φ. **(B)** The variation in polarization angles θ_{qL} and θ_{qT} of the metascreens with central angle φ. **(C)** The variation in normalized impedance Z_{eff}/Z_w and polarization factor η of the metascreens with central angle φ.

central angle φ in the range 0°–230°. Here the same material with identical filling rate Φ and beam thickness t, are unchanged as the third Section. To explain the underwater sound insulation mechanism of the metascreens in Figure 2A, Figure 4 shows the effective parameters of the metascreens with different central angles φ calculated using the homogenization method.

As shown in Figure 4A, a significant decrease in the phase velocity of the qL wave c_{qL} from 3935.48 m/s to 116.70 m/s is observed as the central angle φ increases. In addition, the phase velocity of the qT wave c_{qT} also drops from 330.58 m/s to 55.12 m/s. Figure 4B shows that the polarization angle amplitude of the qL wave θ_{qL}, obviously increases with the central angle φ. Conversely, the polarization angle of the qT wave θ_{qT}, decreases with increasing central angle φ. Both θ_{qL} and θ_{qT} gradually deviate from their respective pure wave modes (θ_{qL} = 0°; θ_{qT} = 90°).

Figure 4C shows that, the effective acoustic impedance Z_{eff} of the metascreen can be significantly reduced by increasing the central angle φ, and shows a similar trend as c_{qL}. According to Eq. 14, in addition to the substantial decrease in c_{qL}, the slight reduction in the polarization factor η (from 0.999 to 0.814) also further contributes to achieving the extremely low effective acoustic impedance Z_{eff} (from 1.5238 Z_w to 0.0369 Z_w) of the metascreen.

To clearly show the effective parameters variations in Figure 4; Table 2 presents the effective parameters of the four metascreens embedded with chiral structures having central

TABLE 2 Effective parameters of four metascreens.

φ/(°)	c_{qL}/(m/s)	c_{qT}/(m/s)	θ_{qL}/(°)	θ_{qT}/(°)	Z_{eff}/Z_w	η
0	3935.48	330.58	0	89.93	1.5238	0.999
150	632.29	179.81	-15.76	74.24	0.2036	0.843
190	297.76	110.05	-20.54	69.46	0.0944	0.826
230	116.70	55.12	-26.83	63.13	0.0369	0.814

angles $\varphi = 0°$, 150°, 190° and 230°. In general, the sound insulation performance of the metascreen at low frequency can be significantly improved with a decrease in the phase velocity of the qL wave c_{qL}, or the effective acoustic impedance Z_{eff}, induced by an acoustic impedance mismatch between the metascreen and surrounding water.

The displacement deformation fields for A190 and A230 are investigated to explain the formation of their transmission coefficient peaks and valleys in Figure 2A. As shown in Figures 5A,B, at the transmission valley frequency, the displacement along the x-axis on the right side of both metascreens A190 and A230 is much weaker than that of the left side. This weakness is verified by the average absolute displacement (AAD) of the metascreen transmission dip frequency denoted by the two red curves in Figures 5C,D. The AAD of the x component on the right side of the metascreens reaches a minimum and has a lower displacement magnitude than on the left side. However, at the transmission peak frequency, the displacement of the x component on the left side of the metascreens is almost equal to the right side, which can also be verified by the red curves in Figures 5C,D.

One can also see from Figure 5 that the displacement along the y-axis on both sides of the metascreens A190 and A230 at the transmission dip frequency is weaker than that at the transmission peak frequency. Indeed, the metascreen transmission peaks is induced by Fabry Pérot (FP) resonance, which is excited by the extremely low velocity of the qT wave. The overall thickness of the metascreens is

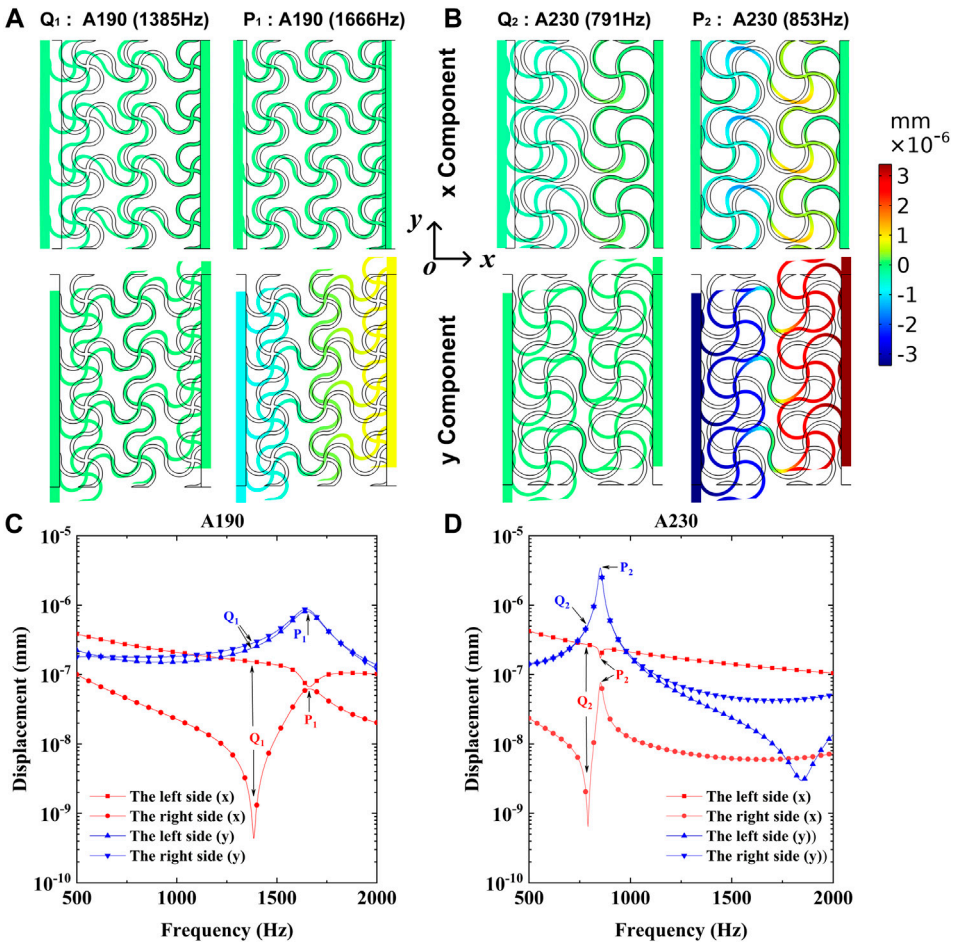

FIGURE 5
(A,B) are the displacement deformation fields at the transmission peak and valley frequencies, **(C)** and **(D)** are the average absolute displacements of the x and y components for metascreens A190 and A230, respectively.

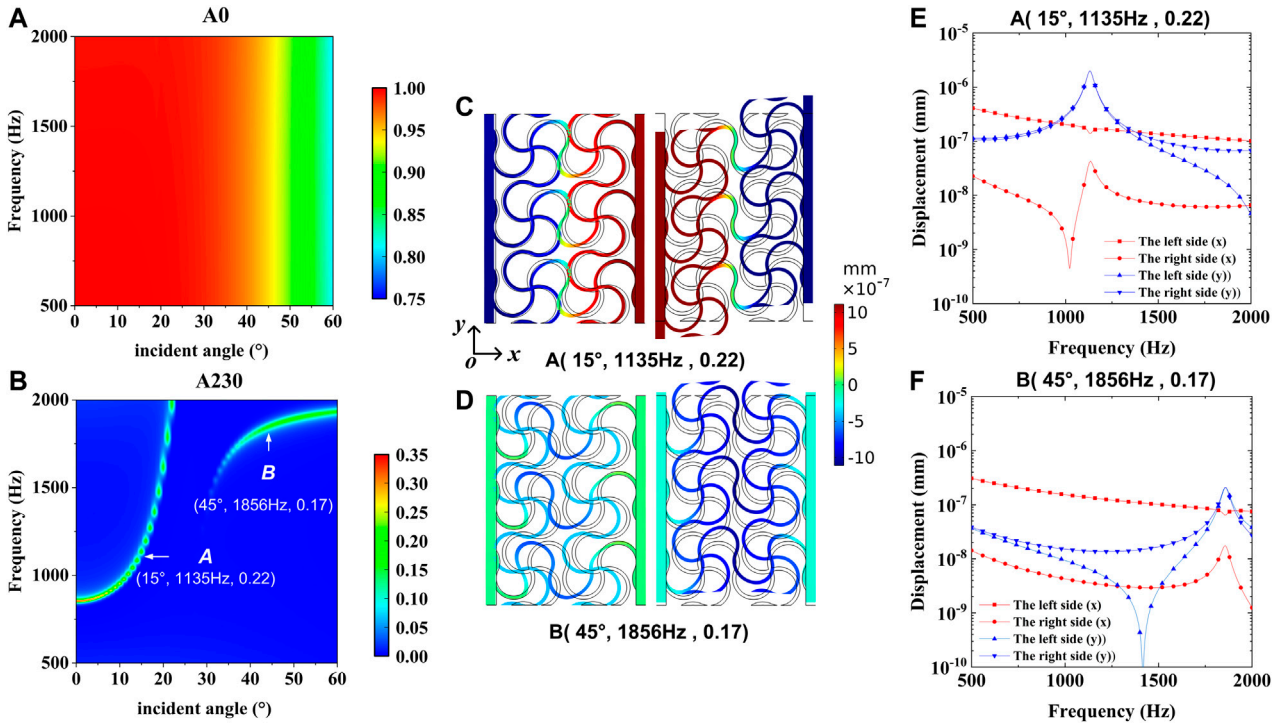

FIGURE 6
(A,B) are the acoustic transmission coefficients for metascreens A0 and A230, respectively, versus the incidence angle and frequency. **(C,D)** are the displacement fields at the transmission peak frequency points of A230 at 15° and 45° incidence angles, respectively. **(E)** and **(F)** show the average absolute displacement of A230 in the *x* and *y* components at 15° and 45° incidence angles, respectively.

around a half-wavelength of the qT wave ($t_{ms} \approx \frac{c_{qT}}{2f}$), which satisfies the FP resonance excitation condition (Lu et al., 2007; Li et al., 2013).

Finally, Figure 6 shows the effect of oblique incidence angle on the sound transmission coefficients for metascreens A0 and A230. One can see that A0 is almost transparent for waterborne sound at various oblique incidences (Figure 6A), although the transmission coefficient decreases to 0.8 at the 60° incidence angle. However, A230 maintains good underwater sound insulation performance at different oblique incidences (Figure 6B). Note that a new weak transmission peak appears when the incidence angle is above 28°. The displacement fields and the AAD can again interpret the underlying mechanisms of the A230 transmission peaks. Figures 6C–F show the displacement fields and the AAD for incidence angles of 15° and 45°. At the incidence angle of 15°, the displacement field and the AAD are similar to those at the normal incidence. The minimum displacement along the *x*-axis on the right side of the metascreen A230 at 1,022 Hz (Figure 6E) induces the transmission dip and the maximum displacement at 1,135 Hz means a transmission peak. For the displacement fields and the AAD of the incidence angle of 45°, there is an obvious displacement peak along the *x*-axis on the right side at 1856 Hz (Figure 6E), which induce a noticeable transmission peak. However, there is no obvious dip of displacement along the *x* axis on the right side, and all the AAD along the *x*-axis on the right side is relative weak except 1856 Hz. In short, the metascreen A230 shows wideband sound insulation.

Conclusion

The anisotropic chiral aluminum lattice is introduced to construct a metascreen for low-frequency underwater sound insulation. The results show that the metascreen transmission coefficient decreases noticeably in the low and broad frequency range with the degree of chirality for the same filling rate. The average transmission coefficient can be lowered to 0.0145 in the frequency range of 500–2000 Hz.

The effective acoustic properties of different metascreens are investigated using the homogenization method. It is found that an extensive quasi-longitudinal wave phase velocity range from 116.70 m/s to 3935.48 m/s can be obtained by adjusting the central angle without changing the filling rate. In addition, lower effective sound velocity and effective acoustic impedance of the metascreen can be achieved by increasing the degree of chirality, which contributes to low-frequency sound insulation.

The sound insulation mechanism is further investigated through the displacement pattern and effective acoustic impedance. The low phase velocity of the quasi-longitudinal

wave and low polarization factor collectively lead to the low effective acoustic impedance of the metascreen. It is also shown that the shear resonance related to the extremely low phase velocity of the quasi-transverse wave results in the metascreen transmission peak.

The effect of oblique incidence angle on the metascreen's sound insulation ability is also investigated, and the good sound insulation performance of the A230 metascreen is generally robust at different incidence angles. Overall, this study paves a promising avenue for anisotropic chiral structures with applications to underwater sound insulation.

Data availability statement

The original contributions presented in the study are included in the article/supplementary material, further inquiries can be directed to the corresponding authors.

Author contributions

CW: Writing-original draft preparation, software, writing-review and editing. YW and HZ: Software, writing-review and editing. JZ, HY, DY, and JW: Writing-review and editing, supervision.

Funding

This work is supported by NSFC (Grant Nos. 52171327, 11991032, and 51805537).

Conflict of interest

The authors declare that the research was conducted in the absence of any commercial or financial relationships that could be construed as a potential conflict of interest.

Publisher's note

All claims expressed in this article are solely those of the authors and do not necessarily represent those of their affiliated organizations, or those of the publisher, the editors and the reviewers. Any product that may be evaluated in this article, or claim that may be made by its manufacturer, is not guaranteed or endorsed by the publisher.

References

An, X., Lai, C., He, W., and Fan, H. (2021). Three-dimensional chiral meta-plate lattice structures for broad band vibration suppression and sound absorption. *Compos. Part B Eng.* 224, 109232. doi:10.1016/j.compositesb.2021.109232

Bensoussanand Alain (1978). *Asymptotic analysis for periodic structures/*. North-Holland Pub. Co.

Cai, Z., Zhao, S., Huang, Z., Li, Z., Su, M., Zhang, Z., et al. (2019). Bubble architectures for locally resonant acoustic metamaterials. *Adv. Funct. Mat.* 29, 1906984. doi:10.1002/adfm.201906984

Calvo, D. C., Thangawng, A. L., Layman, J. C. N., Casalini, R., and Othman, S. F. (2015). Underwater sound transmission through arrays of disk cavities in a soft elastic medium. *J. Acoust. Soc. Am.* 138, 2537–2547. doi:10.1121/1.4931446

Chen, Y., Zhao, B., Liu, X., and Hu, G. (2020a). Highly anisotropic hexagonal lattice material for low frequency water sound insulation. *Extreme Mech. Lett.* 40, 100916. doi:10.1016/j.eml.2020.100916

Chen, Z., Yan, F., Negahban, M., and Li, Z. (2020b). Resonator-based reflective metasurface for low-frequency underwater acoustic waves. *J. Appl. Phys.* 128, 055305. doi:10.1063/5.0006523

Cheng, G., Cai, Y., and Xu, L. (2013). Novel implementation of homogenization method to predict effective properties of periodic materials. *Acta Mech. Sin.* 29, 550–556. doi:10.1007/s10409-013-0043-0

Dong, H. W., Zhao, S. D., Miao, X. B., Shen, C., Cheng, L., Zhao, Z., et al. (2021). Customized broadband pentamode metamaterials by topology optimization. *J. Mech. Phys. Solids* 152, 104407. doi:10.1016/j.jmps.2021.104407

Hladky-Hennion, A. C., and Decarpigny, J. N. (1991). Analysis of the scattering of a plane acoustic wave by a doubly periodic structure using the finite element method: Application to Alberich anechoic coatings. *J. Acoust. Soc. Am.* 90, 3356–3367. doi:10.1121/1.401395

Lakes, R. S., Plesha, M, E., Li, J., and Chan, S. H. (2015). Controllable thermal expansion of large magnitude in chiral negative Poisson's ratio lattices. *Phys. Status Solidi B* 252, 1431–1434. doi:10.1002/pssb.201552158

Lanoy, M., Guillermic, R. M., Strybulevych, A., and Page, J. H. (2018). Broadband coherent perfect absorption of acoustic waves with bubble meta-screens. *Appl. Phys. Lett.* 113, 171907. doi:10.1063/1.5051341

Leroy, V., Strybulevych, A., Lanoy, M., Lemoult, F., Tourin, A., and Page, H. J. (2015). Super-absorption of acoustic waves with bubble meta-screens. *Phys. Rev. B* 91, 020301(R). doi:10.1103/PhysRevB.91.020301

Leroy, V., Strybulevych, A., Scanlon, M. G., and Page, J. H. (2009). Transmission of ultrasound through a single layer of bubbles. *Eur. Phys. J. E* 29, 123–130. doi:10.1140/epje/i2009-10457-y

Li, Y., Liang, B., Zou, X., and Cheng, J. (2013). Extraordinary acoustic transmission through ultrathin acoustic metamaterials by coiling up space. *Appl. Phys. Lett.* 103, 063509. doi:10.1063/1.4817925

Liu, J., Yan, D., Pang, W., and Zhang, Y. (2021). Design, fabrication and applications of soft network materials. *Mat. TodayKidlingt.* 49, 324–350. doi:10.1016/j.mattod.2021.05.007

Lu, M., Liu, X., Feng, L., Li, J., Huang, C., Chen, Y., et al. (2007). Extraordinary acoustic transmission through a 1D grating with very narrow apertures. *Phys. Rev. Lett.* 99, 174301. doi:10.1103/PhysRevLett.99.174301

Wang, Y., Zhao, H., Yang, H., Liu, J., Yu, D., and Wen, J. (2022). Topological design of lattice materials with application to underwater sound insulation. *Mech. Syst. Signal Process.* 171, 108911. doi:10.1016/j.ymssp.2022.108911

Wu, H., Hao, C., and Zhang, H. (2020). Underwater broadband sound insulation with chiral spiral structures. *AIP Adv.* 10, 125022. doi:10.1063/5.0025486

Wu, W., Hu, W., Qian, G., Liao, H., Xu, X., and Berto, F. (2019). Mechanical design and multifunctional applications of chiral mechanical metamaterials: A review. *Mat. Des.* 180, 107950. doi:10.1016/j.matdes.2019.107950

Yang, H., Xiao, Y., Zhao, H., Zhong, J., and Wen, J. (2019). On wave propagation and attenuation properties of underwater acoustic screens consisting of periodically perforated rubber layers with metal plates. *J. Sound. Vib.* 444, 21–34. doi:10.1016/j.jsv.2018.12.031

Yin, Y., Zhao, Z., and Li, Y. (2021). Theoretical and experimental research on anisotropic and nonlinear mechanics of periodic network materials. *J. Mech. Phys. Solids* 152, 104458. doi:10.1016/j.jmps.2021.104458

Zhang, Y., Wen, J., Zhao, H., Yu, D., Cai, L., and Wen, X. (2013). Sound insulation property of membrane-type acoustic metamaterials carrying different masses at adjacent cells. *J. Appl. Phys.* 114, 063515. doi:10.1063/1.4818435

Zhao, B., Wang, D., Zhou, P., Liu, X., and Hu, G. (2022). Design of load-bearing materials for isolation of low-frequency waterborne sound. *Phys. Rev. Appl.* 17, 034065. doi:10.1103/PhysRevApplied.17.034065